CHEMISTRY

Unraveling the long-pursued Au_{144} structure by x-ray crystallography

Nan Yan[1,2], Nan Xia[1,2], Lingwen Liao[1,2], Min Zhu[1,2], Fengming Jin[1,2], Rongchao Jin[3]*, Zhikun Wu[1,2]*

The transition from nanocluster to nanocrystal is a central issue in nanoscience. The atomic structure determination of metal nanoparticles in the transition size range is challenging and particularly important in understanding the quantum size effect at the atomic level. On the basis of the rationale that the intra- and interparticle weak interactions play critical roles in growing high-quality single crystals of metal nanoparticles, we have reproducibly obtained ideal crystals of $Au_{144}(SR)_{60}$ and successfully solved its structure by x-ray crystallography (XRC); this structure was theoretically predicted a decade ago and has long been pursued experimentally but without success until now. Here, XRC reveals an interesting Au_{12} hollow icosahedron in thiolated gold nanoclusters for the first time. The Au–Au bond length, close to that of bulk gold, shows better thermal extensibility than the other Au–Au bond lengths in $Au_{144}(SR)_{60}$, providing an atomic-level perspective because metal generally shows better thermal extensibility than nonmetal materials. Thus, our work not only reveals the mysterious, long experimentally pursued structure of a transition-sized nanoparticle but also has important implications for the growth of high-quality, single-crystal nanoparticles, as well as for the understanding of the thermal extensibility of metals from the perspective of chemical bonding.

INTRODUCTION

For metal nanoparticles, two regimes are of particular interest, that is, nanocrystals (typically 3 to 100 nm) and nanoclusters (ranging from subnanometer to ~2 nm) (*1*–*4*). The transition from nanoclusters to nanocrystals is a central issue in nanoscience (*5*). Therefore, the atomic structure determination of metal nanoparticles in the transition size range is of high significance for understanding the evolution from nanoclusters to nanocrystals, as well as the quantum size effect at the atomic level. However, the atomic structure determination is generally very challenging (*6*). Beginning in 2007, when the atomic structure of $Au_{102}(SR)_{44}$ (where SR = thiol) was resolved (*7*), more than a dozen metal nanoclusters have been structurally solved (*8*–*15*); however, the structures of metal nanoclusters in the transition region have rarely been reported (*16*–*18*). In particular, the real structure of $Au_{144}(SR)_{60}$ has long remained mysterious (*19*). Although nanoclusters of larger or smaller sizes than $Au_{144}(SR)_{60}$ have been structurally solved by x-ray crystallography (XRC), the structure of $Au_{144}(SR)_{60}$ remains undetermined by XRC since precise determination of its formula by electrospray ionization mass spectrometry (ESI-MS) nearly a decade ago (*20*–*22*). Efforts to elucidate the structure of $Au_{144}(SR)_{60}$ have continued over the past decade. In 2009, Lopez-Acevedo *et al.* (*23*) proposed a structural model based on density functional theory (DFT) simulations, which was backed up by the subsequent x-ray absorption spectroscopic analysis by MacDonald *et al.* (*24*) and Yamazoe *et al.* (*25*), nuclear magnetic resonance by Wong *et al.* (*26*), and scanning transmission electron microscopy studies by Bahena *et al.* (*27*). The proposed symmetric structure indicated that the nanoparticle should not be difficult to crystallize. Several groups acquired crystals of Au_{144} nanoparticles with various ligands, including phenylethanethiolate (PET; $-SC_2H_4Ph$) and para-mercaptobenzoic acid (*p*-MBA) (*28*, *29*). Koivisto *et al.* (*28*) even observed strong diffraction patterns by small-angle x-ray diffraction (XRD), although they failed to do so by large-angle XRD, indicating that they obtained crystals with orientational disorders of the nanoparticles. Evidence of the disorder in the PET ligand layer of the nanoparticles was also observed in infrared (IR) spectroscopy analysis (*28*).

Despite tremendous efforts devoted to the crystal growth of $Au_{144}(SR)_{60}$ nanoparticles, it has long been questionable whether fine crystals of sufficient quality for XRC analysis could be obtained. On the basis of the previous work, we rationalize that the intra- and interparticle weak interactions should play critical roles in the crystal growth (*18*). On one hand, the intraparticle interactions lead to the assembled ligands on the surface of the nanoparticle and restrict the motion of the ligands; on the other hand, the interparticle interactions facilitate the ordered arrangement (assembly) of the nanoparticles and reduce the movement of the nanoparticles in the crystal. To make adequate intra- and interparticle weak interactions, the nature of the ligand, especially the rigidity, should be carefully considered. For example, too much flexibility in the ligands may lead to incompact intra- and interparticle interactions, while too much rigidity in the ligands may inhibit the formation of some intra- and interparticle interactions. This may at least partly explain why high-quality single crystals are difficult to obtain when Au_{144} is protected by either flexible PET or rigid *p*-MBA (*28*, *29*). Therefore, we conclude that a ligand with rigidity falling between the flexible PET and the rigid *p*-MBA may be a resolution of the major problem that high-quality single crystals of $Au_{144}(SR)_{60}$ have been difficult to produce for a decade. In this work, using $PhCH_2SH$ as the protecting ligand, we have now successfully grown single crystals of $Au_{144}(SR)_{60}$ and determined its structure by XRC, which confirms the "compact" and "adequate" intra- and inter-nanoparticle weak interactions as described above. Notably, other factors such as the purification of the product by preparative thin-layer chromatography (PTLC) (*30*) and the selection of suitable conditions for crystal growth also contributed to the successful production of single crystals of $Au_{144}(SR)_{60}$.

[1]Key Laboratory of Materials Physics, Anhui Key Laboratory of Nanomaterials and Nanostructures, CAS Center for Excellence in Nanoscience, Institute of Solid State Physics, Chinese Academy of Sciences, Hefei 230031, P. R. China. [2]Institute of Physical Science and Information Technology, Anhui University, Hefei 230601, P. R. China. [3]Department of Chemistry, Carnegie Mellon University, Pittsburgh, PA 15213, USA. *Corresponding author. Email: zkwu@issp.ac.cn (Z.W.); rongchao@andrew.cmu.edu (R.J.)

RESULTS

The $Au_{144}(SR)_{60}$ nanoparticles were prepared via a reported one-step method (*31*). Briefly, chloroauric acid was first mixed with tetraoctylammonium bromide (TOABr) and excess thiol ($PhCH_2SH$) in methanol to form Au(I)-SR polymers. Then, Au(I)-SR was reduced by sodium borohydride (aqueous solution) to form nanoparticles. After a size-focusing process lasting for ~4.5 hours, the precipitated product was washed with methanol and isolated using PTLC. The $Au_{144}(SCH_2Ph)_{60}$ product was confirmed by ESI-MS (see fig. S1). Triangular prism-like single crystals were grown by vapor diffusion of acetonitrile into a toluene solution of the purified nanoparticles over 1 week at room temperature (fig. S2). As a close comparison, block-like crystals of PET-protected $Au_{144}(PET)_{60}$ were also grown in the same manner but were unfortunately unresolvable (fig. S3), similar to earlier reports by others (*28*), despite the fact that $Au_{144}(PET)_{60}$ shows a similar atomic structure as that of $Au_{144}(SCH_2Ph)_{60}$ according to powder XRD (fig. S4). More experimental details are given in Materials and methods.

The ultraviolet-visible (UV-vis) absorption spectrum of the crystallized $Au_{144}(SCH_2Ph)_{60}$ [redissolved in dichloromethane (DCM)] shows two prominent peaks at 355 and 715 nm, with two inconspicuous humps at 475 and 595 nm (fig. S5), indicating the nonplasmonic nature of the $Au_{144}(SCH_2Ph)_{60}$ nanoparticles (*5*). It is worth noting that the absorption peaks of the redissolved crystals of $Au_{144}(SCH_2Ph)_{60}$ are more distinct than the solution of the amorphous solids of $Au_{144}(SCH_2Ph)_{60}$, probably because of the small-molecule impurities not identified by mass spectroscopy (see fig. S1). The observed red shift of the absorption peaks of $Au_{144}(SCH_2Ph)_{60}$ compared with the peaks of $Au_{144}(PET)_{60}$ is attributed to the ligand effect (*32*). The structure of $Au_{144}(SCH_2Ph)_{60}$ is solved by XRC analysis at 153 K with 0.84-Å resolution, which reveals that the crystal of $Au_{144}(SCH_2Ph)_{60}$ belongs to the trigonal crystal system and adopts a space group of *P*-31*c* (R_1 value of 5.98%; see tables S1 and S2). Such a highly symmetrical packing is not seen in other nanoparticle crystals, except for that of $Au_{60}S_6(SCH_2Ph)_{36}$, in which the nanoparticles form a 6H left-handed helical arrangement (*33*). Note that according to the reported results, large nanoclusters always crystallize in a triclinic or monoclinic space group (*16*–*18*). Figure 1A shows the total structure of $Au_{144}(SCH_2Ph)_{60}$ with the metal core diameter of ~1.7 nm and the entire nanoparticle diameter (including the surface ligand shell) of ~2.9 nm, consistent with the previous report (*27*). Figure 1B presents the two enantiomers of the $Au_{144}(SCH_2Ph)_{60}$ nanoparticle, and the parallel hexahedron unit cell contains a racemic pair.

The as-obtained structure has high symmetry with 6 C_5 rotation axes, 10 C_3 rotation axes, and 15 C_2 rotation axes, as shown in fig. S6, similar to the Pd_{145} structure reported by Tran *et al.* (*34*), except for the following distinct differences: (i) the central vacancy, which reduces the metal atom count from 145 to 144, and (ii) the profound chirality in the outermost shell(s). The crystal structure matches the model proposed by Lopez-Acevedo, especially the most recent theoretical optimizations (*35*, *36*), which demonstrate that the proposed structures have the *I*-symmetry (the 60 Au and 60 S-C shells), resembling the traditional "football" of Asia, although the trigonal (D_3) symmetry imposed by the unit cell was not shown (*37*). This level of agreement between the calculations and the experiment is remarkable. The magnitude of the chirality is also very close to the calculation from the model structure by Pelayo *et al.* (*38*). It is worth noting that the theoretical modeling of this structure type, as

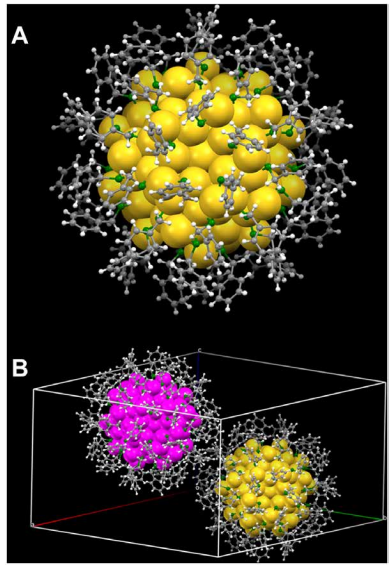

Fig. 1. Total atomic structure of the $Au_{144}(SCH_2Ph)_{60}$ nanoparticle resolved by XRC. (**A**) Dextroisomer of $Au_{144}(SCH_2Ph)_{60}$. Yellow, gold; green, sulfur; gray, carbon; white, hydrogen. (**B**) Parallel hexahedron unit cell containing a pair of enantiomers. The left- and right-handed enantiomers are colored in magenta and yellow, respectively.

used to account for many observed properties of $Au_{144}(SR)_{60}$ and related systems, was motivated directly by the Pd_{145} structure with 60 bridging carbonyl ligands (*34*) because of the agreement in the powder XRD patterns obtained on the samples, along with the knowledge of the precise mass and the composition (*20*–*22*). Of note, the work of Lopez-Acevedo *et al.* (*23*) did not predict the structure, but rather assumed its correctness, and attempted to refine it using the DFT methods, which were finally efficient enough to optimize such a large system. Below, we discuss the details of the structure of the $Au_{144}(SR)_{60}$ nanoparticle.

As shown in Fig. 2A, the inner shell is a hollow 12-atom icosahedron. This is the first experimental observation of a hollow icosahedron (Au_{12}) in thiolated gold nanoparticles, although a similar Ag_{12} icosahedron was observed before (*12*, *13*). In contrast to the hollow structure, the center-filled M_{13} icosahedron is very common in gold, silver, palladium, and platinum nanoclusters (*8*, *9*, *14*, *39*). A plausible speculation of the central vacancy is that the hollow structure significantly relieves the intrinsic strain associated with the Mackay icosahedral packing (*23*). With regard to the analogous Pd_{145}, the palladium atom with its smaller size may accommodate the intrinsic strain. However, unexpectedly, even for the similar-sized $Au_{133}(SR)_{52}$, a center-filled Au_{13} icosahedron was observed (*16*, *17*). It is known that $Au_{144}(SR)_{60}$ can be transformed to $Au_{133}(SR)_{52}$, which prompts the following question: How can a single gold atom enter the center of the hollow Au_{12} icosahedron (*16*, *17*)? This needs to be clarified in future work. It is worth noting that a truncated decahedral core structure of $Au_{144}(SR)_{60}$ has been recently determined by atomic pair distribution function analysis of x-ray powder diffraction data (*40*), and an approximate face-centered cubic (fcc) packing of gold atoms with local variation has also been observed by aberration-corrected electron microscopy in 3-mercaptobenzoic acid–protected $Au_{144}(m\text{-MBA})_{40}$ nanoparticles (*41*, *42*). In addition, Vergara *et al.* (*43*) have reported the crystal structure of a $Au_{146}(p\text{-MBA})_{57}$ nanocluster, which unexpectedly has a twinned fcc

metal core. The structural differences between these comparable sizes of gold nanoclusters are not odd and are likely attributed to the differences in ligands and synthetic protocols because these factors are known to influence the kinetics and thermodynamics of the formation of the final product(s), as adequately demonstrated by our previous work (*10*, *44*, *45*), among which we even obtained a pair of structural isomers by slightly tuning the synthesis conditions (*10*).

Another interesting finding is that the average Au–Au bond length in the hollow M_{12} core is only 2.748 Å (see fig. S7), which is much smaller than the normal Au–Au bond length found in gold nanoparticles (including nanoclusters and nanocrystals) (*16*–*18*). The second layer is composed of 42 gold atoms, forming a 54-atom Mackay icosahedral structure with the hollow Au_{12} core (54-MI) and exhibiting 20 triangular (111) faces (Fig. 2B), rather than the 55-MI in the reported Pd_{145} and Au_{133} structures. Then, 60 gold atoms enclose the 54-MI and assemble into a rhombicosidodecahedron (Fig. 2C), which was previously observed in the Pd_{145} nanoparticle (*34*). The surface of this polyhedron consists of 12 pentagons and 20 equilateral triangles. The centers of the 12 pentagons correspond to the vertices of 54-MI, and a triangular (111) face covers each face of 54-MI in a hexagonal close-packed (hcp) packing mode. The shared vertexes of the pentagons and the triangles on the rhombicosidodecahedron form 30 parallelograms [not squares as predicted (*23*)], on which 30 (RS-Au-SR) staples ride astride, giving rise to the complete $Au_{144}(SR)_{60}$ structure (Fig. 2, D and F). The anatomy of the Au_{114} kernel is shown in Fig. 2E, indicating an *a*-*b*-*c* layer stacking. In previous reports, the Au–Au bonds in and between each shell were believed to be equivalent (*24*). However, detailed analyses (fig. S7) demonstrate that multiple kinds of Au–Au bond lengths exist in $Au_{144}(SCH_2Ph)_{60}$, implying a transition state of $Au_{144}(SCH_2Ph)_{60}$ from nanoclusters to nanocrystals in view of the chemical bonding. For example, the average Au–Au bond lengths in the pentagons and triangles of the *c* layer are 3.217 and 2.884 Å, respectively (the shorter bonds of the triangle's edges presumably arise from the steric strain, which was also found in Pd_{145}); the Au–Au bond length in the *b* layer is 2.914 Å. The bond length of 2.884 Å (one type of bond in layer c) is close to that of bulk gold, indicating that the Au_{144} nanoparticle has some metal character, while the other bond lengths indicate that the nanoparticle has some nonmetal character. Note that, although the shell-by-shell (*a*-*b*-*c*, 12-42-60) construction and chiral assembly of 30 monomeric (S-Au-S) staple motifs on the surface of Au_{114} have been correctly proposed theoretically (*23*), the Au–Au bond lengths in the first and second shells predicted by the calculation have deviations from the experimental results [first shell, 2.845 (theory)/2.748 (experiment) Å; second shell, 3.010 (theory)/2.914 (experiment) Å], and unfortunately, the detailed Au–Au bond length in the third shell was not provided in the theoretical work. In addition, the staple motifs in the theoretically proposed structure were oriented in an arbitrary manner such that the total structural symmetry was undefined. A detailed comparison between the present solved structure and the structure proposed by Lopez-Acevedo *et al.* is shown in fig. S8. The range of Au–Au distances in the kernel of Au_{144} is similar to the one reported by Azubel *et al.* (*46*) for $Au_{68}(3\text{-MBA})_{32}$. In that work, an unexpected optical gap of 2500 cm^{-1} was shown in the IR spectrum of $Au_{68}(3\text{-MBA})_{32}$. The $Au_{144}(SCH_2Ph)_{60}$ seems to show a gap at ~750 cm^{-1}, as seen in fig. S9.

To stabilize the large Au_{114} core, 30 monomeric (S-Au-S) staple motifs are distributed on the surface of the Au_{114} core with highly ordered patterns. From the side view shown in Fig. 3A, the staples self-assemble into an annulus pattern, which can be divided into three parts (marked with different colors): The 5-membered rings with 5 staple motifs near the poles of the Au_{114} kernel are marked in red; the 10-membered ring consisting of 10 staple motifs on the equator is marked in yellow, and the remaining two 5-membered rings located in the midlatitude regions of the Au_{114} core are marked in blue. From the top view (Fig. 3B), the five-membered ring looks similar to a pentagonal ripple, and the red and blue rings are arranged in opposite rotary directions. All five rings surround a fivefold axis across the two opposite pentagons. Note that the Au_{60} rhombicosidodecahedron has 12 pentagons and six fivefold axes (*27*, *35*). Thus, each fivefold axis can be encompassed by five rings (Fig. 3C). Moreover, the 10-membered ring on the equator can be separated into two alternate sets: One set consists of the five parallel staples along the fivefold axis, and the other deviates from the equator. Meanwhile, the five parallel staples can be regarded as the vertices of a penta-star (Fig. 3D). In another view, the 30 staples can also be grouped into six penta-stars. The reverse orientations of the five

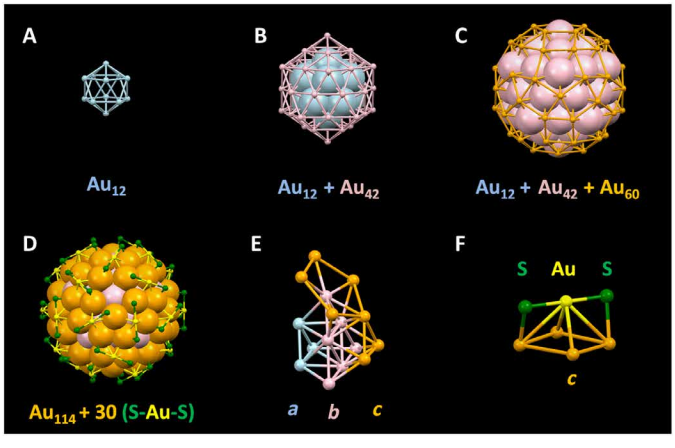

Fig. 2. Dissection of the $Au_{144}(SCH_2Ph)_{60}$ atomic structure. (**A**) Inner icosahedral shell of 12 Au atoms (light blue). (**B**) Middle icosahedral shell of 42 Au atoms (pink). (**C**) Outer rhombicosidodecahedron shell of 60 Au atoms (orange). (**D**) Thirty (SR-Au-SR) staples containing 30 Au atoms (yellow) and 60 sulfur atoms (green). (**E**) Three-layered Au_{114} core with an *a*-*b*-*c* structure. (**F**) Isolated (SR-Au-SR) staple astride the parallelogram on the Au_{60} shell. Alkyl groups are omitted for clarity.

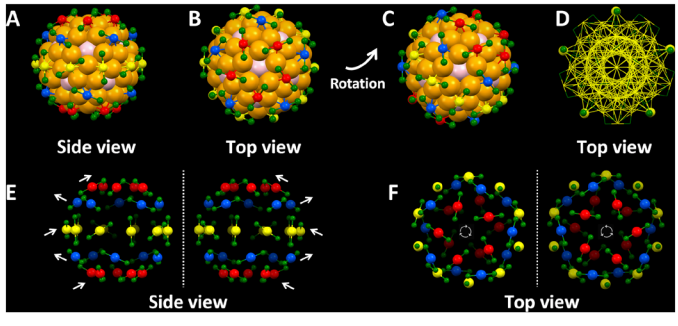

Fig. 3. Self-assembly mode of surface (SR-Au-SR) staples. (**A**) Side view, (**B**) top view, and (**C**) rotated view of the ring-like assembled staples on the surface; different groups of gold atoms are colored in red, blue, and yellow, respectively. (**D**) Exhibition of the five paralleled staples at the vertex peaks of a penta-star. (**E**) Side view and (**F**) top view of the chiral ring-like assembled staples. The white arrows indicate the orientation of each ring. Alkyl groups are omitted for clarity.

rings give rise to the chirality of the $Au_{144}(SCH_2Ph)_{60}$ nanoparticle (Fig. 3E), and a pair of enantiomers are presented in Fig. 3F. In contrast, the monomeric (S-Au-S) staple motifs in Au_{144} are replaced by triethylphosphine ligands directly connected to the outermost 30 palladium atoms, and the assumed 60 CO groups (disordered in the crystal) bridge the palladium atoms on the edges of Pd_{145} (*34*). Thus, Pd_{145} does not exhibit the chirality found in Au_{144}. To sum up, the Au_{144} structure shares some similarities with Pd_{145}, but there are distinct differences as well.

As mentioned in Introduction, the intra- and internanoparticle interactions were proposed to play critical roles in the crystal growth (*18*). Here, we found the weak interactions in the crystal. As shown in Fig. 4A, the H···H interaction exists between the hydrogen atoms of two adjacent benzenes in the same staple, evidenced by their very close distance (2.545 and 2.837 Å, respectively; see fig. S10A) and the similar inward orientation of the two adjacent benzenes. In addition to the H···H interaction, the C-H···π intraparticle interaction also exists, and the H···π distance is short (average, 2.80 Å; see Fig. 4B and fig. S10B) (*18*). These interactions lead to the reverse spiral arrangements of the two sets of benzene rings in the staple ring (inside and outside, five benzenes for each set), shown in fig. S10C, which was not previously reported. As a consequence, these interactions enable every single nanoparticle to be compacted and ordered with reduced intraparticle vibration, contributing to the formation of high-quality single crystals.

In addition to the intraparticle interactions, interparticle interactions are also found at the interface of neighboring $Au_{144}(SCH_2Ph)_{60}$ nanoparticles. As shown in Fig. 5 (A and B), the enantiomers are packed into different layers and organized into a square superlattice in the (100) and (010) planes. A hexagonal pattern can be observed in the (001) plane (Fig. 5C), with each $Au_{144}(SR)_{60}$ nanoparticle being wrapped by six equivalent anti-chiral nanoparticles (Fig. 5D).

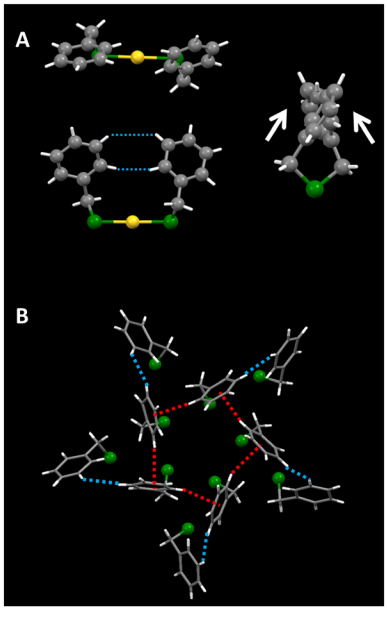

Fig. 4. Self-assembly mode analysis of surface ligands. (**A**) Different direction views of monomeric (SR-Au-SR) staple. The white arrows point in the orientation of the benzene ring. Yellow, gold; green, sulfur; gray, carbon; white, hydrogen. (**B**) Weak interactions between the interacted 10 ligands. Red dashed lines, C-H···π interaction; blue dashed lines, H···H interaction.

When the interface of two adjacent nanoparticles is magnified, six thiolates are found enwound by both C-H···π and H···H interactions, which act as a "clip" to fix the interface ligands and the neighboring nanoparticles, finally leading to the formation of an ordered superlattice (Fig. 5, E and F, and fig. S11) (*18*).

We reproduced the structure by analyzing another single crystal obtained in another synthesized batch, demonstrating the reliability of our experimental results. The reliable structure provides a prerequisite to investigating the thermodynamic influence on the structure of the $Au_{144}(SCH_2Ph)_{60}$ nanoparticles. As shown in fig. S12 and tables S3 to S6, the structural framework is essentially unchanged as the temperature increases from 100 K (0.84-Å resolution) to 243 K (0.83-Å resolution). However, the Au–Au bond length changes are distinctly observed when the temperature rises from 100 to 243 K. All Au–Au bond lengths in the Au_{114} core elongate more or less as the temperature increases. More specifically, the Au–Au bonds in the inner shell elongate from 2.748 to 2.758 Å, and the Au–Au bonds in the second shell elongate from 2.917 to 2.922 Å. The two kinds of Au–Au bonds in the third shell stretch from 3.220 to 3.224 Å and 2.883 to 2.895 Å, respectively. The small-angle XRD analysis also qualitatively reveals that the distance between the two neighboring nanoparticles in the amorphous powder enlarges as the temperature increases, indicating that the nanoparticles expand with the temperature rise (fig. S13). An interesting finding is that the Au–Au bonds with a length close to that of bulk gold (2.88 Å) have the largest elongation (+0.41%), indicating that this kind of bond has better thermal extensibility than the shorter or longer ones, which may provide the atomic-level perspective for the fact that metals generally show better thermal extensibility than nonmetal solid materials.

It came to our attention during the revision of this manuscript that Lei *et al.* (*47*) recently reported a Au_{144} structure protected by alkynyl ligands. The two Au_{144} nanoparticles have a similar kernel but different staple motifs due to the ligand difference. The averaged Au–Au bond lengths in the shells of the kernel are also slightly different (first shell, 2.755/2.748 Å; second shell, 2.912/2.914 Å; third shell, 3.162/3.220 and 2.946/2.883 Å; alkynyl-protected/thiolate-protected Au_{144}). Besides, the total structure of $Au_{144}(C{\equiv}CAr)_{60}$

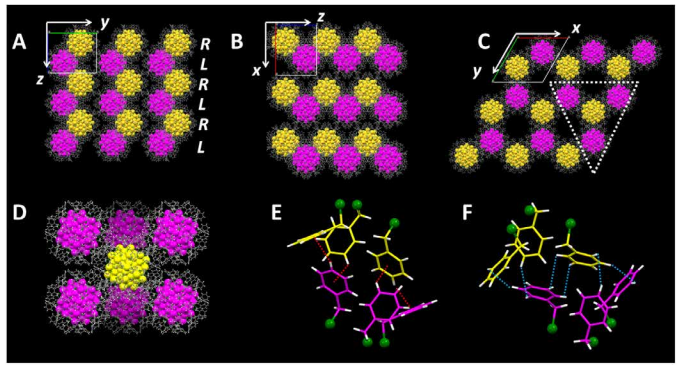

Fig. 5. Self-assembly mode analysis of packing nanoparticles in a crystal. (**A**) View of the superlattice from the *x* axis, (**B**) *y* axis, and (**C**) *z* axis. (**D**) Packing of a dextroisomer with the six nearest levoisomers. Magenta and yellow, gold atoms in left- and right-handed enantiomers; green, sulfur; gray, carbon; white, hydrogen. (**E** and **F**) Weak interactions between ligands in neighboring nanoparticles. Magenta and yellow, carbon atoms in left- and right-handed enantiomers; green, sulfur; white, hydrogen. Red dashed lines, C-H···π interaction; blue dashed lines, H···H interaction.

(Ar = 2-F-C_6H_4-) does not exhibit the *I*-symmetry of $Au_{144}(SCH_2Ph)_{60}$ because of the asymmetry of the C≡CAr ligand. The $Au_{144}(SCH_2Ph)_{60}$ differs from $Au_{144}(C{\equiv}CAr)_{60}$ not only in ligand composition and surface structure but also in the material properties (for example, optical absorption). Furthermore, $Au_{144}(C{\equiv}CAr)_{60}$ is a new species and does not involve the historical long pursuit of the thiolated Au_{144} nanoparticle. Finally, the intra- and internanoparticle interactions, temperature-dependent Au–Au bond length, etc., are not involved in the work of Lei *et al*.

DISCUSSION

In summary, we have reproducibly grown ideal single crystals of the $Au_{144}(SR)_{60}$ nanoparticle and resolved its structure using XRC on the basis of designed intra- and interparticle weak interactions, as these play critical roles in growing high-quality single crystals of metal nanoparticles. XRC also reveals a multiplicity of Au–Au bond lengths in the kernel of $Au_{144}(SR)_{60}$, indicating that $Au_{144}(SR)_{60}$ is a transition size in terms of Au–Au bonding character. It is found that the Au–Au bond with the length close to that of bulk gold shows the best thermal extensibility among various Au–Au bonds in the $Au_{144}(SR)_{60}$ nanoparticle, which provides an atomic-level perspective for the fact that metals generally show better thermal extensibility than nonmetal solid materials. The significance and novelty of our work include the following: (i) We resolved a structure that has perplexed the scientific community for nearly a decade since its composition determination by ESI-MS. (ii) The available structure will pave the way for future research of structure-property correlation, transition-sized nanoparticles, etc. (iii) We provided important implications and guidance for the challenging single-crystal growth of metal nanoparticles. (iv) This work also provided an atomic-level perspective for the good thermal extensibility of metals compared with other common nonmetal solid materials.

MATERIALS AND METHODS

Materials

Tetrachloroauric(III) acid ($HAuCl_4{\cdot}4H_2O$, >99.9% metal basis), TOABr (≥98.0%), phenylethanethiol (99%, Sigma-Aldrich), benzyl mercaptane (99%, Sigma-Aldrich), 4-*tert*-butylbenzylmercaptan (99%, Sigma-Aldrich), *p*-methylphenylthiophenol (99%, Sigma-Aldrich), 2,4-dimethylbenzenethiol (99%, Sigma-Aldrich), and sodium borohydride ($NaBH_4$, 99.8%, Shanghai Chemical Reagent Co. Ltd.) were used. Ethanol, toluene, acetonitrile, *n*-pentane, CH_2Cl_2, and methanol were purchased from Sinopharm Chemical Reagent Co. Ltd. The water used in all experiments was ultrapure (resistivity, 18.2 megohms·cm), produced by a Milli-Q NANO pure water system. All chemicals were used as received.

Synthesis of $Au_{144}(SR)_{60}$

The synthesis of $Au_{144}(SR)_{60}$ nanoclusters is documented in a previous work and modified here (*31*). All the reactions were conducted at room temperature under ambient air. Typically, $HAuCl_4{\cdot}4H_2O$ (0.607 mmol, 250 mg) and TOABr (0.696 mmol, 380 mg) were added to a 100-ml single-neck round-bottom flask and mixed with 30 ml of methanol. After being vigorously stirred for 30 min, the solution color changed from yellow to dark red. Then, various thiols (3.19 mmol for each synthesis) were added to the solution at room temperature. A milky, white floc was generated immediately. After ~15 min, a fresh $NaBH_4$ solution (6 mmol, 227 mg, dissolved in 10 ml of nanopure water) was rapidly added to the solution under vigorous stirring. The color of the solution immediately turned black and produced Au particles, which were precipitated out of the methanol solution. The reaction was stopped after ~4.5 hours, and then the solution was removed. Black precipitates were washed with excess methanol and collected by centrifugation. This wash/precipitation procedure was repeated several times. The crude products that were dissolved in 1 ml of CH_2Cl_2 were pipetted onto eight pieces of a PTLC plate (10 cm by 20 cm), and the separation was conducted in a developing tank (solvent: DCM/petroleum ether = 20:20, v/v) for ~5 min. Then, the band of $Au_{144}(SCH_2Ph)_{60}$ in the PTLC plate was cut, and the nanoparticles were extracted with pure DCM and then dried by rotary evaporation. The yield of $Au_{144}(SCH_2Ph)_{60}$ was 16% (on an Au atom basis). After trying various solutions and precipitants, it was determined that single crystals of $Au_{144}(SCH_2Ph)_{60}$ could be acquired by vapor diffusion of acetonitrile into a toluene solution of $Au_{144}(SCH_2Ph)_{60}$ over 1 week at room temperature. The synthesis and crystal growth of other thiolated Au_{144} compounds were conducted in the same manner.

Characterization

ESI mass spectra were recorded on a Waters QTof mass spectrometer using a Z-spray source. The sample was first dissolved in toluene (~0.5 mg/ml) and then diluted (2:1, v/v) with an ethanol solution that contained 50 mmol CsOAc. The sample was directly infused into the chamber at 5 μl/min. The source temperature was kept at 70°C, the spray voltage was 2.20 kV, and the cone voltage was adjusted to 60 V. XRD data were collected with an X'Pert PRO MPD (PANalytical) diffractometer using Cu Kα as the radiation source at 40 kV and 40 mA. All UV/vis/near-IR absorption spectra were acquired in the range of 190 to 900 nm using a UV2600 spectrophotometer. The single-crystal XRD data were collected on a Bruker D8 VENTURE PHOTON 100 CMOS diffractometer with HELIOS MX multilayer monochromator Cu Kα radiation (λ = 1.54178 Å). The structure and phase purity were checked by a Rigaku-TTR3 x-ray diffractometer using high-intensity graphite monochromatized Cu Kα radiation. Fourier transform IR spectra were acquired on a Nicolet 8700 spectrometer. The small-angle XRD patterns at selected temperatures were registered to investigate the structural phase transition, where the variation in temperature was realized by using a closed He-gas cycle refrigerator installed on the x-ray diffractometer.

SUPPLEMENTARY MATERIALS

Supplementary material for this article is available at http://advances.sciencemag.org/cgi/content/full/4/10/eaat7259/DC1

Fig. S1. ESI-MS analysis of $Au_{144}(SCH_2Ph)_{60}$.
Fig. S2. Photograph of triangular prism-shaped $Au_{144}(SCH_2Ph)_{60}$ crystals.
Fig. S3. Photograph (partly marked with red circle) and single-crystal diffraction pattern of $Au_{144}(PET)_{60}$ amorphous solid.
Fig. S4. XRD patterns of $Au_{144}(SCH_2Ph)_{60}$ and $Au_{144}(SC_2H_4Ph)_{60}$ powders.
Fig. S5. UV-vis absorption spectra of $Au_{144}(SCH_2Ph)_{60}$ nanoparticles redissolved in solutions of amorphous and crystalline $Au_{144}(SCH_2Ph)_{60}$ solids and crystalline $Au_{144}(SC_2H_4Ph)_{60}$ solid.
Fig. S6. The atomic structure of $Au_{144}(SCH_2Ph)_{60}$ viewed along different symmetry axes.
Fig. S7. The statistics of different types of Au–Au bonds and Au–S bonds of $Au_{144}(SCH_2Ph)_{60}$.
Fig. S8. A detailed comparison between the present solved structure of $Au_{144}(SCH_2Ph)_{60}$ and the structure proposed by Lopez-Acevedo *et al*.
Fig. S9. IR spectrum of $Au_{144}(SCH_2Ph)_{60}$.
Fig. S10. The weak interactions between surface ligands and the chirally assembled pattern.
Fig. S11. The weak interactions between surface ligands in neighboring nanoparticles.

Fig. S12. The statistics and increasing proportion of the Au–Au bond in different shells of the Au_{114} core resolved at 100 and 243 K, respectively.
Fig. S13. Small-angle XRD patterns of amorphous $Au_{144}(SCH_2Ph)_{60}$ powder at selected temperatures.
Table S1. Crystal data and structure refinement for $Au_{144}(SCH_2Ph)_{60}$ at 153 K (sample 1).
Table S2. Atomic coordinates and equivalent isotropic displacement parameters for $Au_{144}(SCH_2Ph)_{60}$ at 153 K (sample 1).
Table S3. Crystal data and structure refinement for $Au_{144}(SCH_2Ph)_{60}$ at 100 K (sample 2).
Table S4. Atomic coordinates and equivalent isotropic displacement parameters for $Au_{144}(SCH_2Ph)_{60}$ at 100 K (sample 2).
Table S5. Crystal data and structure refinement for $Au_{144}(SCH_2Ph)_{60}$ at 243 K (sample 2).
Table S6. Atomic coordinates and equivalent isotropic displacement parameters for $Au_{144}(SCH_2Ph)_{60}$ at 243 K (sample 2).

REFERENCES AND NOTES

1. X. Wang, J. Zhuang, Q. Peng, Y. Li, A general strategy for nanocrystal synthesis. *Nature* **437**, 121–124 (2005).
2. N. L. Rosi, C. A. Mirkin, Nanostructures in biodiagnostics. *Chem. Rev.* **105**, 1547–1562 (2005).
3. R. Jin, C. Zeng, M. Zhou, Y. Chen, Atomically precise colloidal metal nanoclusters and nanoparticles: Fundamentals and opportunities. *Chem. Rev.* **116**, 10346–10413 (2016).
4. I. Chakraborty, T. Pradeep, Atomically precise clusters of noble metals: Emerging link between atoms and nanoparticles. *Chem. Rev.* **117**, 8208–8271 (2017).
5. Y. Negishi, T. Nakazaki, S. Malola, S. Takano, Y. Niihori, W. Kurashige, S. Yamazoe, T. Tsukuda, H. Häkkinen, A critical size for emergence of nonbulk electronic and geometric structures in dodecanethiolate-protected Au clusters. *J. Am. Chem. Soc.* **137**, 1206–1212 (2015).
6. S. Billinge, I. Levin, The problem with determining atomic structure at the nanoscale. *Science* **316**, 561–565 (2007).
7. P. D. Jadzinsky, G. Calero, C. J. Ackerson, D. A. Bushnell, R. D. Kornberg, Structure of a thiol monolayer-protected gold nanoparticle at 1.1 Å resolution. *Science* **318**, 430–433 (2007).
8. M. Zhu, C. M. Aikens, F. J. Hollander, G. C. Schatz, R. Jin, Correlating the crystal structure of a thiol-protected Au_{25} cluster and optical properties. *J. Am. Chem. Soc.* **130**, 5883–5885 (2008).
9. M. W. Heaven, A. Dass, P. S. White, K. M. Holt, R. W. Murray, Crystal structure of the gold nanoparticle $[N(C_8H_{17})_4][Au_{25}(SCH_2CH_2Ph)_{18}]$. *J. Am. Chem. Soc.* **130**, 3754–3755 (2008).
10. S. Tian, Y.-Z. Li, M.-B. Li, J. Yuan, J. Yang, Z. Wu, R. Jin, Structural isomerism in gold nanoparticles revealed by X-ray crystallography. *Nat. Commun.* **6**, 8667 (2015).
11. X.-K. Wan, Z.-W. Lin, Q.-M. Wang, Au_{20} nanocluster protected by hemilabile phosphines. *J. Am. Chem. Soc.* **134**, 14750–14752 (2012).
12. A. Desireddy, B. E. Conn, J. Guo, B. Yoon, R. N. Barnett, B. M. Monahan, K. Kirschbaum, W. P. Griffith, R. L. Whetten, U. Landman, T. P. Bigioni, Ultrastable silver nanoparticles. *Nature* **501**, 399–402 (2013).
13. H. Yang, Y. Wang, H. Huang, L. Gell, L. Lehtovaara, S. Malola, H. Häkkinen, N. Zheng, All-thiol-stabilized Ag_{44} and $Au_{12}Ag_{32}$ nanoparticles with single-crystal structures. *Nat. Commun.* **4**, 2422 (2013).
14. L. G. AbdulHalim, M. S. Bootharaju, Q. Tang, S. Del Gobbo, R. G. AbdulHalim, M. Eddaoudi, D.-e. Jiang, O. M. Bakr, $Ag_{29}(BDT)_{12}(TPP)_4$: A tetravalent nanocluster. *J. Am. Chem. Soc.* **137**, 11970–11975 (2015).
15. N. Yan, L. Liao, J. Yuan, Y.-j. Lin, L.-h. Weng, J. Yang, Z. Wu, Bimetal doping in nanoclusters: Synergistic or counteractive? *Chem. Mater.* **28**, 8240–8247 (2016).
16. C. Zeng, Y. Chen, K. Kirschbaum, K. Appavoo, M. Y. Sfeir, R. Jin, Structural patterns at all scales in a nonmetallic chiral $Au_{133}(SR)_{52}$ nanoparticle. *Sci. Adv.* **1**, e1500045 (2015).
17. A. Dass, S. Theivendran, P. R. Nimmala, C. Kumara, V. R. Jupally, A. Fortunelli, L. Sementa, G. Barcaro, X. Zuo, B. C. Noll, $Au_{133}(SPh\text{-}tBu)_{52}$ nanomolecules: X-ray crystallography, optical, electrochemical, and theoretical analysis. *J. Am. Chem. Soc.* **137**, 4610–4613 (2015).
18. C. Zeng, Y. Chen, K. Kirschbaum, K. J. Lambright, R. Jin, Emergence of hierarchical structural complexities in nanoparticles and their assembly. *Science* **354**, 1580–1584 (2016).
19. T. G. Schaaff, M. N. Shafigullin, J. T. Khoury, I. Vezmar, R. L. Whetten, Properties of a ubiquitous 29 kDa Au:SR cluster compound. *J. Phys. Chem. B* **105**, 8785–8796 (2001).
20. N. K. Chaki, Y. Negishi, H. Tsunoyama, Y. Shichibu, T. Tsukuda, Ubiquitous 8 and 29 kDa gold:alkanethiolate cluster compounds: Mass-spectrometric determination of molecular formulas and structural implications. *J. Am. Chem. Soc.* **130**, 8608–8610 (2008).
21. H. Qian, R. Jin, Controlling nanoparticles with atomic precision: The case of $Au_{144}(SCH_2CH_2Ph)_{60}$. *Nano Lett.* **9**, 4083–4087 (2009).
22. C. A. Fields-Zinna, R. Sardar, C. A. Beasley, R. W. Murray, Electrospray ionization mass spectrometry of intrinsically cationized nanoparticles, $[Au_{144/146}(SC_{11}H_{22}N(CH_2CH_3)_3^+)_x(S(CH_2)_5CH_3)_y]^{x+}$. *J. Am. Chem. Soc.* **131**, 16266–16271 (2009).
23. O. Lopez-Acevedo, J. Akola, R. L. Whetten, H. Grönbeck, H. Häkkinen, Structure and bonding in the ubiquitous icosahedral metallic gold cluster $Au_{144}(SR)_{60}$. *J. Phys. Chem. C* **113**, 5035–5038 (2009).
24. M. A. MacDonald, P. Zhang, H. Qian, R. Jin, Site-specific and size-dependent bonding of compositionally precise gold–thiolate nanoparticles from X-ray spectroscopy. *J. Phys. Chem. Lett.* **1**, 1821–1825 (2010).
25. S. Yamazoe, S. Takano, W. Kurashige, T. Yokoyama, K. Nitta, Y. Negishi, T. Tsukuda, Hierarchy of bond stiffnesses within icosahedral-based gold clusters protected by thiolates. *Nat. Commun.* **7**, 10414 (2016).
26. O. A. Wong, C. L. Heinecke, A. R. Simone, R. L. Whetten, C. J. Ackerson, Ligand symmetry-equivalence on thiolate protected gold nanoclusters determined by NMR spectroscopy. *Nanoscale* **4**, 4099–4102 (2012).
27. D. Bahena, N. Bhattarai, U. Santiago, A. Tlahuice, A. Ponce, S. B. H. Bach, B. Yoon, R. L. Whetten, U. Landman, M. Jose-Yacaman, STEM electron diffraction and high-resolution images used in the determination of the crystal structure of the $Au_{144}(SR)_{60}$ cluster. *J. Phys. Chem. Lett.* **4**, 975–981 (2013).
28. J. Koivisto, K. Salorinne, S. Mustalahti, T. Lahtinen, S. Malola, H. Häkkinen, M. Pettersson, Vibrational perturbations and ligand–layer coupling in a single crystal of $Au_{144}(SC_2H_4Ph)_{60}$ nanocluster. *J. Phys. Chem. Lett.* **5**, 387–392 (2014).
29. C. J. Ackerson, P. D. Jadzinsky, J. Z. Sexton, D. A. Bushnell, R. D. Kornberg, Synthesis and bioconjugation of 2 and 3 nm-diameter gold nanoparticles. *Bioconjugate Chem.* **21**, 214–218 (2010).
30. L. Liao, C. Yao, C. Wang, S. Tian, J. Chen, M.-B. Li, N. Xia, N. Yan, Z. Wu, Quantitatively monitoring the size-focusing of Au nanoclusters and revealing what promotes the size transformation from $Au_{44}(TBBT)_{28}$ to $Au_{36}(TBBT)_{24}$. *Anal. Chem.* **88**, 11297–11301 (2016).
31. H. Qian, R. Jin, Ambient synthesis of $Au_{144}(SR)_{60}$ nanoclusters in methanol. *Chem. Mater.* **23**, 2209–2217 (2011).
32. X. Yuan, B. Zhang, Z. Luo, Q. Yao, D. T. Leong, N. Yan, J. Xie, Balancing the rate of cluster growth and etching for gram-scale synthesis of thiolate-protected Au_{25} nanoclusters with atomic precision. *Angew. Chem. Int. Ed.* **53**, 4623–4627 (2014).
33. Z. Gan, J. Chen, J. Wang, C. Wang, M.-B. Li, C. Yao, S. Zhuang, A. Xu, L. Li, Z. Wu, The fourth crystallographic closest packing unveiled in the gold nanocluster crystal. *Nat. Commun.* **8**, 14739 (2017).
34. N. T. Tran, D. R. Powell, L. F. Dahl, Nanosized $Pd_{145}(CO)_X(PEt_3)_{30}$ containing a capped three-shell 145-atom metal-core geometry of pseudo icosahedral symmetry. *Angew. Chem. Int. Ed.* **39**, 4121–4125 (2000).
35. H.-Ch. Weissker, H. B. Escobar, V. D. Thanthirige, K. Kwak, D. Lee, G. Ramakrishna, R. L. Whetten, X. López-Lozano, Information on quantum states pervades the visible spectrum of the ubiquitous $Au_{144}(SR)_{60}$ gold nanocluster. *Nat. Commun.* **5**, 3785 (2014).
36. H.-Ch. Weissker, O. Lopez-Acevedo, R. L. Whetten, X. López-Lozano, Optical spectra of the special Au_{144} gold-cluster compounds: Sensitivity to structure and symmetry. *J. Phys. Chem. C* **119**, 11250–11259 (2015).
37. A. Tlahuice-Flores, D. M. Black, S. B. H. Bach, M. Jose-Yacaman, R. L. Whetten, Structure & bonding of the gold-subhalide cluster $I\text{-}Au_{144}Cl_{60}^{[2]}$. *Phys. Chem. Chem. Phys.* **15**, 19191–19195 (2013).
38. J. J. Pelayo, R. L. Whetten, I. L. Garzón, Geometric quantification of chirality in ligand-protected metal clusters. *J. Phys. Chem. C* **119**, 28666–28678 (2015).
39. E. G. Mednikov, M. C. Jewell, L. F. Dahl, Nanosized $(\mu_{12}\text{-}Pt)Pd_{164-x}Pt_x(CO)_{72}(PPh_3)_{20}$ ($x \approx 7$) containing Pt-centered four-shell 165-atom Pd-Pt core with unprecedented intershell bridging carbonyl ligands: Comparative analysis of icosahedral shell-growth patterns with geometrically related $Pd_{145}(CO)_x(PEt_3)_{30}$ ($x \approx 60$) containing capped three-shell Pd_{145} core. *J. Am. Chem. Soc.* **129**, 11619–11630 (2007).
40. K. M. Ø. Jensen, P. Juhas, M. A. Tofanelli, C. L. Heinecke, G. Vaughan, C. J. Ackerson, S. J. L. Billinge, Polymorphism in magic-sized $Au_{144}(SR)_{60}$ clusters. *Nat. Commun.* **7**, 11859 (2016).
41. M. Azubel, A. L. Koh, K. Koyasu, T. Tsukuda, R. D. Kornberg, Structure determination of a water-soluble 144-gold atom particle at atomic resolution by aberration-corrected electron microscopy. *ACS Nano* **11**, 11866–11871 (2017).
42. T.-R. Tero, S. Malola, B. Koncz, E. Pohjolainen, S. Lautala, S. Mustalahti, P. Permi, G. Groenhof, M. Pettersson, H. Häkkinen, Dynamic stabilization of the ligand–metal interface in atomically precise gold nanoclusters Au_{68} and Au_{144} protected by *meta*-mercaptobenzoic acid. *ACS Nano* **11**, 11872–11879 (2017).
43. S. Vergara, D. A. Lukes, M. W. Martynowycz, U. Santiago, G. Plascencia-Villa, S. C. Weiss, M. J. de la Cruz, D. M. Black, M. M. Alvarez, X. López-Lozano, C. O. Barnes, G. Liu, H.-C. Weissker, R. L. Whetten, T. Gonen, M. J. Yacaman, G. Calero, MicroED structure of $Au_{146}(p\text{-}MBA)_{57}$ at subatomic resolution reveals a twinned FCC cluster. *J. Phys. Chem. Lett.* **8**, 5523–5530 (2017).
44. Y. Chen, C. Zeng, D. R. Kauffman, R. Jin, Tuning the magic size of atomically precise gold nanoclusters via isomeric methylbenzenethiols. *Nano Lett.* **15**, 3603–3609 (2015).
45. Z. Wu, M. A. MacDonald, J. Chen, P. Zhang, R. Jin, Kinetic control and thermodynamic selection in the synthesis of atomically precise gold nanoclusters. *J. Am. Chem. Soc.* **133**, 9670–9673 (2011).
46. M. Azubel, J. Koivisto, S. Malola, D. Bushnell, G. L. Hura, A. L. Koh, H. Tsunoyama, T. Tsukuda, M. Pettersson, H. Häkkinen, R. D. Kornberg, Electron microscopy of gold nanoparticles at atomic resolution. *Science* **345**, 909–912 (2014).

47. Z. Lei, J.-J. Li, X.-K. Wan, W.-H. Zhang, Q.-M. Wang, Isolation and total structure determination of an all-alkynyl-protected gold nanocluster Au_{144}. *Angew. Chem. Int. Ed.* **57**, 8639–8643 (2018).

Acknowledgments: A portion of this work was performed on the Steady High Magnetic Field Facilities, High Magnetic Field Laboratory, CAS. We thank L. Zhang for the discussion of XRD pattern. **Funding:** This work was supported by the National Natural Science Foundation of China (nos. 21501181, 21829501, 21222301, 21771186, 21603234, 21701179, 21528303, and 21171170), Key Program of 13th Five-Year Plan, CASHIPS (KP-2017-16), Director Foundation of ISSP (no. 2016DFY05), Innovative Program of Development Foundation of Hefei Center for Physical Science and Technology (2017FXCX002), and CAS/SAFEA International Partnership Program for Creative Research Teams. **Author contributions:** N.Y. synthesized the nanoparticles and grew the crystals. N.X. and L.L. carried out the structural analysis. M.Z. and F.J. helped synthesize the nanoparticles. Z.W. and R.J. designed the study, supervised the project, and analyzed the data. All authors contributed to the preparation of the manuscript. **Competing interests:** The authors declare that they have no competing interests. **Data and materials availability:** All data needed to evaluate the conclusions in the paper are present in the paper and/or the Supplementary Materials. Additional data related to this paper may be requested from the authors.

Submitted 28 March 2018
Accepted 31 August 2018
Published 12 October 2018
10.1126/sciadv.aat7259

Citation: N. Yan, N. Xia, L. Liao, M. Zhu, F. Jin, R. Jin, Z. Wu, Unraveling the long-pursued Au_{144} structure by x-ray crystallography. *Sci. Adv.* **4**, eaat7259 (2018).

ScienceAdvances

Unraveling the long-pursued Au_{144} structure by x-ray crystallography

Nan Yan, Nan Xia, Lingwen Liao, Min Zhu, Fengming Jin, Rongchao Jin and Zhikun Wu

Sci Adv **4** (10), eaat7259.
DOI: 10.1126/sciadv.aat7259